
03 Jan 2023

Rotation-Inversion Isomerization of Tertiary Carbamates: Potential Energy Surface Analysis of Multi-Paths Isomerization using Boltzmann Statistics

Brian Jameson

Rainer Glaser

Missouri University of Science and Technology, glaserr@mst.edu

Follow this and additional works at: https://scholarsmine.mst.edu/chem_facwork

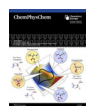
 Part of the [Chemistry Commons](#)

Recommended Citation

B. Jameson and R. Glaser, "Rotation-Inversion Isomerization of Tertiary Carbamates: Potential Energy Surface Analysis of Multi-Paths Isomerization using Boltzmann Statistics," *ChemPhysChem*, vol. 24, no. 1, article no. e202200442, Wiley, Jan 2023.

The definitive version is available at <https://doi.org/10.1002/cphc.202200442>

This Article - Journal is brought to you for free and open access by Scholars' Mine. It has been accepted for inclusion in Chemistry Faculty Research & Creative Works by an authorized administrator of Scholars' Mine. This work is protected by U. S. Copyright Law. Unauthorized use including reproduction for redistribution requires the permission of the copyright holder. For more information, please contact scholarsmine@mst.edu.



Rotation-Inversion Isomerization of Tertiary Carbamates: Potential Energy Surface Analysis of Multi-Paths Isomerization Using Boltzmann Statistics

Brian Jameson^[a] and Rainer Glaser^{*[a]}

Potential energy surface (PES) analyses at the SMD[MP2/6–311++G(d,p)] level and higher-level energies up to MP4(fc,SDTQ) are reported for the fluorinated tertiary carbamate *N*-ethyl-*N*-(2,2,2-trifluoroethyl) methyl carbamate (**VII**) and its parent system *N,N*-dimethyl methyl carbamate (**VI**). Emphasis is placed on the analysis of the rotational barrier about the CN carbamate bond and its interplay with the hybridization of the *N*-lone pair (NLP). All rotational transition state (TS) structures were found by computation of 1D relaxed rotational profiles but only 2D PES scans revealed the rotation-inversion paths in a compelling fashion. We found four unique chiral minima of **VII**, one pair each of *E*- and *Z*-rotamers, and we determined the *eight* unique rotational TS structures associated with every possible *E/Z*-isomerization path. It is a significant finding that all TS structures feature *N*-pyramidalization whereas the minima essentially contain sp²-hybridized nitrogen. We will show that

the TS stabilities are affected by the synergetic interplay between NLP/CO₂ repulsion minimization, NLP→σ*(CO) negative hyperconjugation, and two modes of intramolecular through-space electrostatic stabilization. We demonstrate how Boltzmann statistics must be applied to determine the predicted experimental rotational barrier based on the energetics of all eight rotamerization pathways. The computed barrier for **VII** is in complete agreement with the experimentally measured barrier of the very similar fluorinated carbamate *N*-Boc-*N*-(2,2,2-trifluoroethyl)-4-aminobutan-1-ol **II**. NMR properties of **VII** were calculated with a variety of density functional/basis set combinations and Boltzmann averaging over the *E*- and *Z*-rotamers at our best theoretical level results in good agreement with experimental chemical shifts δ(¹³C) and *J*-(¹³C,¹⁹F) coupling constants of **II** (within 6%).

Introduction

The hindered rotation about conjugated R₃–CO–NR₁R₂ amide-type frameworks is among the most studied topics in conformational chemistry and the kinetics of the *E/Z* isomerization between the *N*-sp² hybridized minima has attracted continued attention.^[1–5] Ureas R₄R₃N–CO–NR₁R₂ and carbamates R₃O–CO–NR₁R₂ show similar *E/Z* isomerism. The rotational barrier of parent urea was studied by Stilbs and Forsén,^[6] and Bryantsev et al. determined the rotational barriers for a collection of alkyl substituted urea systems.^[7] Far fewer carbamate systems have been studied in depth.^[8–13]


In the context of our synthetic work on tertiary carbamates we needed to understand their dynamic stereochemistry. While developing syntheses for *N*-trifluoroethyl lysine and derivatives we worked with compounds I–V (Scheme 1). Compound **I** is the unprotected starting material, compounds **II**, **III**, and **IV** are *tert*-butyl carbamate (Boc) protected intermediates, and **V** is the deprotected product. The ¹³C NMR spectra were recorded with ¹³C–¹H decoupling while leaving ¹³C–¹⁹F coupling intact. The spectra are shown in Figure 1 and they feature two quartets for

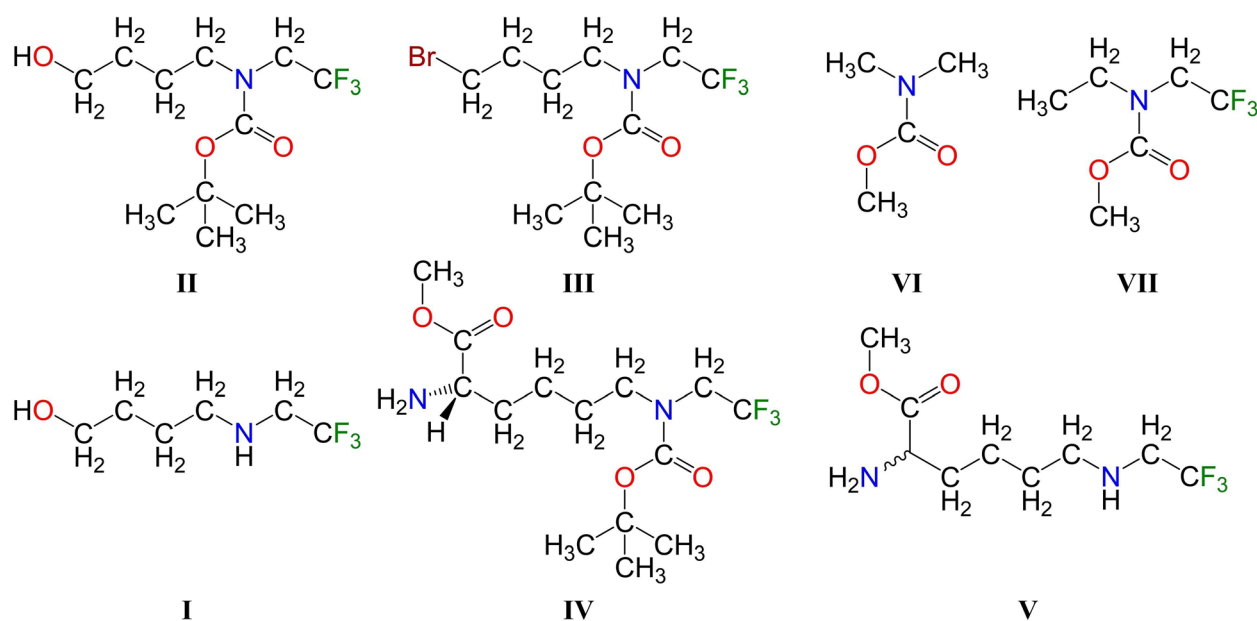
the –CF₃ group of the Boc protected intermediates. Since the two quartets were only detected in the presence of the Boc group, we hypothesized that the two signals were caused by the presence of at least two non-equilibrating isomers.

The CN rotation in amides is essentially independent of the amide *N*-hybridization and the amino group remains more or less sp²-hybridized.^[4] In contrast, CN rotation in carbamate systems is correlated with changes in *N*-hybridization (sp² to sp³) along the isomerization pathways and these isomerizations really are *bone fide* rotation-inversion processes. While there is only one *E*-isomer and one *Z*-isomer of an amide connected by one isomerization path, the stereochemistry of carbamates may allow for *several E*-isomers and *Z*-isomers which are connected by several inversion-rotation pathways. These complicating features of the potential energy surfaces must be taken into account to accurately simulate the measured activation barrier for isomerization.

To understand the nature of these isomers, we studied the parent system **VI** and the model system **VII**. The potential energy surface (PES) of parent system **VI** was explored to create a reference point for the larger fluorinated model system **VII**. The model system **VII** includes the essential structural features of the species in our experimental work including the methyl carbamate framework to imitate the Boc protecting group, a trifluoroethyl group, and an ethyl group as a small alkyl chain. The electronic structure of fluorinated carbamates is complex because they allow for a variety of intramolecular interactions including electrostatic stabilization of the alkyl group and/or

[a] B. Jameson, Prof. Dr. R. Glaser
Department of Chemistry,
Missouri University of Science and Technology
Rolla, Missouri, 65401 (USA)
E-mail: glaser@mst.edu

 Supporting information for this article is available on the WWW under <https://doi.org/10.1002/cphc.202200442>



Scheme 1. Structures of *N*-(2,2,2-trifluoroethyl)-4-aminobutan-1-ol (I), *N*-Boc-*N*-(2,2,2-trifluoroethyl)-4-aminobutan-1-ol (II), *N*^ε-Boc-*N*^ε-(2,2,2-trifluoroethyl)-4-bromobutan-1-amine (III), *N*^ε-Boc-*N*^ε-(2,2,2-trifluoroethyl)-*L*-lysinate (IV), *N*^ε-(2,2,2-trifluoroethyl)-*D,L*-lysine (V), the parent system *N,N*-dimethyl methyl carbamate (VI), and the model system *N*-ethyl-*N*-(2,2,2-trifluoroethyl) methyl carbamate (VII).

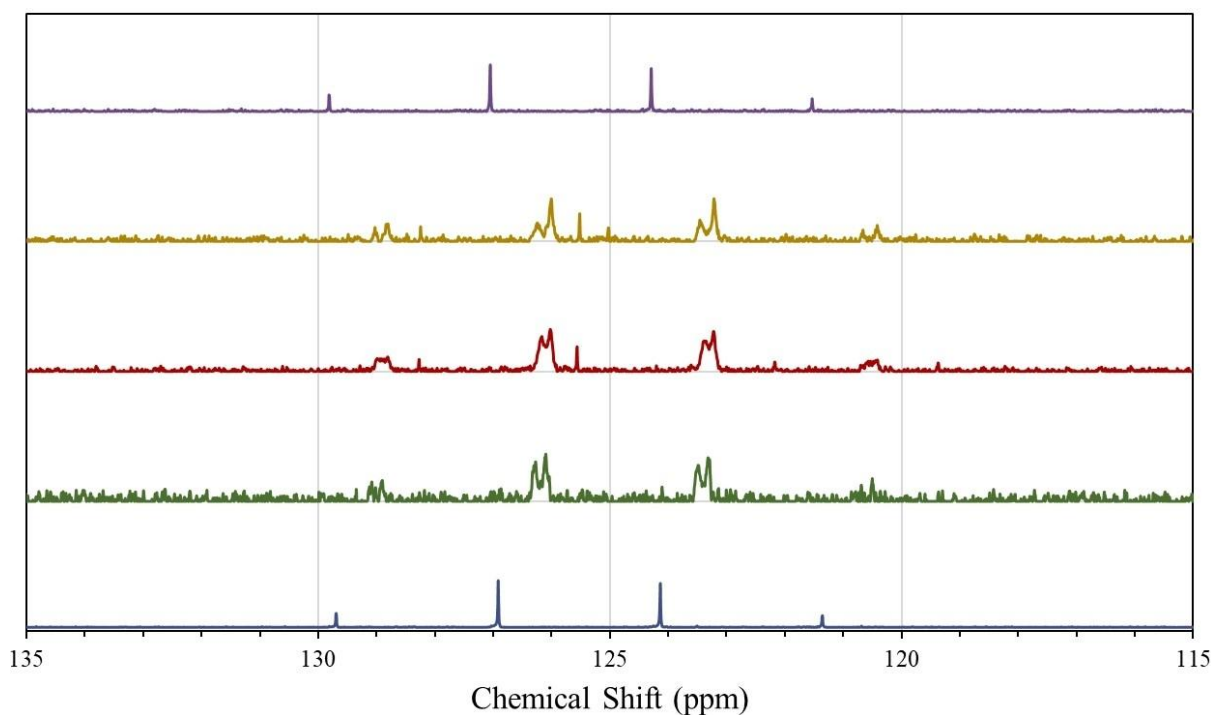


Figure 1. The $-\text{CF}_3$ quartet regions of the experimental ^{13}C NMR spectra of I (blue), II (green), III (red), IV (yellow), and V (purple).

fluoroalkyl group by the carbamate,^[8] and possibly fluorine–oxygen halogen interactions.^[14] The wealth of intramolecular noncovalent interactions requires higher levels of correlated electronic structure theory, and we report results of potential energy surface analysis at the MP2 level with higher energy level energies computed up to full MP4(SDTQ) using a

large basis set. We will present a complete potential energy surface analysis of VII including the characterization of conformational barriers about the *N*-alkyl single bonds.

Our focus will be the determination of the carbamate *E*- and *Z*-rotamers and the rotational barrier between them. The discussion is rendered particularly interesting because the

potential energy surface contains four equilibrium structures of comparable energy: two conformers for each of the *E*- and *Z*-rotamers. The present work coherently describes a consistent and rigorous method for the theoretical prediction of a single experimental rotational barrier resulting from *multi-paths* scenarios. This is accomplished with Boltzmann statistics and the consideration of all *E/Z*-isomerization paths. We will show that the carbamate rotation is correlated with *N*-pyramidalization and 2D PES scans are presented for the full appreciation of the rotation-inversion paths. The best transition state structures resulted from minimization of the electrostatic repulsion between the *N*-lone pair (NLP) and the CO₂ moiety and concomitant NLP→σ*(CO) negative hyperconjugation. The results of the potential energy surface analysis will be connected directly to the experimental NMR data via computed chemical shifts δ(¹³C) and *J*(¹³C,¹⁹F) coupling constants determined at the most suited DFT levels. The computed carbamate rotational barrier of **VII** is compared to the experimentally measured barriers of carbamate ester **II** and related carbamates and contrasted to the barriers in related amides. The results of the present study should be of general interest to chemists working with carbamates, ureas, and related compounds.

Computational Methods

There are two parts to the computational study. The first part involves an extensive potential energy surface analysis to locate all the minima, to explore all pathways for *N*-inversion and bond rotations by scanning appropriate internal coordinates, and the characterization of inversion-rotation via 2D plots of the potential energy surfaces. The second part seeks to establish a direct connection between computed molecular properties and the measured NMR spectra by computation of chemical shifts and ¹³C-¹⁹F coupling constants. With a view to the possible intramolecular interactions in carbamates, we thought it important to explore the potential energy surface with a correlated method that accounts also for dispersion. Therefore, we optimized our systems using second-order Møller-Plesset perturbation theory (MP2) and employed higher-order perturbation theory (MPx) to confirm relative energies. Hartree-Fock and/or DFT methods cannot be fully trusted in studies where electron correlation changes are expected to be large because of CN bond rotation and the associated conjugation change and because non-covalent intramolecular interactions matter. With the structures firmly established, we computed NMR properties using density functional theory (DFT). Computations were performed with Gaussian16^[15] on the Missouri University of Science and Technology high performance computational cluster. 3D surfaces generated from the carbamate rotational profiles were compiled and generated using Wolfram Mathematica.^[16]

Potential Energy Surface Analysis

Møller-Plesset perturbation theory is a post Hartree-Fock computational method that improves on the Hartree-Fock approximation by the addition of electron correlation through Rayleigh-Schrödinger perturbation theory with varying orders of correlation. We utilized second-order Møller-Plesset perturbation theory using the frozen core approximation MP2(fc)^[17,18] for geometry optimizations and for the vibrational analysis. The 6-311++G(d,p) basis set^[19] was used; that is, the triple-zeta basis set 6-311G was augmented with diffuse and polarization functions on all atoms. Potential energy surface analyses were performed for gas phase and with the inclusion of a universal solvation model based on solute electron density,^[20] SMD[MP2(fc)/6-311++G(d,p)] to simulate the chloroform solution from our experimental data. We also computed energies using third- (MP3)^[21] and full fourth-order Møller-Plesset perturbation theory with single (S), double (D), triple (T) and quadruple (Q) excitations using the frozen core approximation (MP4(fc,SDTQ)^[22-24]) with the same basis set and the MP2(fc)/6-311++G(d,p) geometries. The same higher level MPx calculations were performed with the SMD model based on the structures optimized with the SMD level, SMD[MPx/6-311++G(d,p)]//SMD[MP2(fc)/6-311++G(d,p)]. Unless otherwise noted, the structures and energies obtained with SMD solvation are discussed.

Total energies and thermochemical parameters computed at the level of optimization SMD[MP2(fc)/6-311++G(d,p)] are reported in Table 1. The thermochemical properties are reported unscaled. In Table 2 are listed relative energies of **VI** and **VII** computed at the SMD[MPx] level and the Boltzmann populations for the isomers of **VII**. The respective gas phase data is collected in Table S1 and Table S2 in the Supporting Information. Molecular models of the SMD[MP2] stationary structures are shown in Figures 2 and 4 and selected dihedral angles are summarized in Table 3 and Table S3. Cartesian

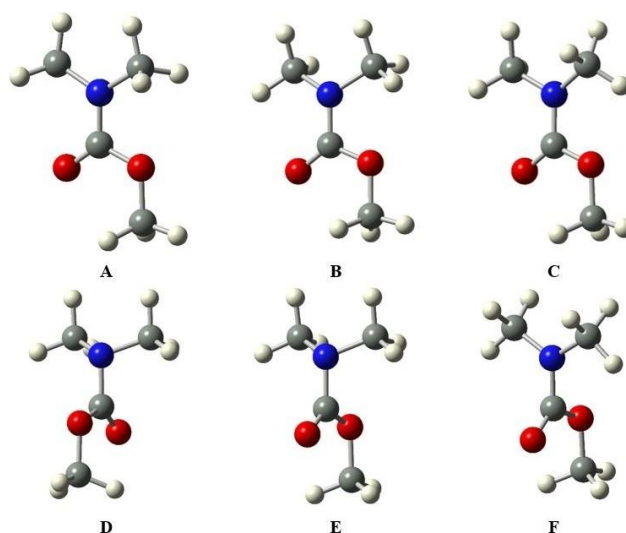


Figure 2. Optimized stationary structures of *N,N*-dimethyl methyl carbamate.

Species	Total E	VZPE	TE	S	ν	U_{298}	G_{298}
A	-362.169033	85.72	90.88	89.37	i164.4	-362.024202	-362.065718
B	-362.170958	86.20	91.55	89.20	102.0	-362.025062	-362.066501
C	-362.169182	85.83	90.92	88.30	70.5	-362.024289	-362.065300
D	-362.148375	85.96	90.59	83.06	i98.2	-362.004017	-362.042538
E	-362.147396	85.81	90.50	83.66	i91.9	-362.003180	-362.041983
F	-362.137695	85.99	90.65	83.33	i97.1	-361.993237	-362.031886
1	-737.832897	107.60	115.70	114.94	41.8	-737.648521	-737.701788
2	-737.833387	107.71	115.75	113.89	47.1	-737.648929	-737.702099
4	-737.832131	107.58	115.66	114.37	38.7	-737.647814	-737.701210
5	-737.832460	107.64	115.70	114.04	41.2	-737.648085	-737.701325
1a	-737.83062	107.60	115.14	109.98	i72.2	-737.647127	-737.698436
1b	-737.830893	107.89	115.86	113.29	42.9	-737.646265	-737.699147
2a	-737.830425	107.70	115.24	110.55	i70.0	-737.646772	-737.698355
2b	-737.830635	107.94	115.93	113.61	40.7	-737.645897	-737.698930
TS(1,4')	-737.826753	107.71	115.20	109.02	i101.7	-737.643169	-737.694023
TS(2,5')	-737.827117	107.68	115.19	109.11	i105.4	-737.643545	-737.694443
TS(1,4)	-737.822786	107.68	115.20	108.09	i69.7	-737.639208	-737.689620
TS(2,5)	-737.823174	107.60	115.14	108.28	i76.0	-737.639687	-737.690191
3a ₁	-737.807051	107.28	114.73	108.29	i69.8	-737.624212	-737.674720
3a ₂	-737.805743	107.45	114.90	109.09	i79.2	-737.622643	-737.673530
3b ₁	-737.807338	107.34	114.81	109.28	i87.4	-737.624370	-737.675348
3b ₂	-737.805424	107.45	114.88	107.74	i78.3	-737.622346	-737.672590
6a ₁	-737.801881	107.14	114.72	109.78	i92.5	-737.619062	-737.670278
6a ₂	-737.812168	107.26	114.77	109.60	i65.8	-737.629277	-737.680408
6b ₁	-737.802847	107.18	114.74	109.69	i88.0	-737.619994	-737.671167
6b ₂	-737.811396	107.29	114.78	109.08	i56.5	-737.628487	-737.679368

[a] All data computed at SMD[MP2/6-311 + + G(d,p)] with scrf=(smd, solvent = chloroform). [b] Total energies (Total E) in Hartree, vibrational zero-point energies (VZPE) and thermal energies (TE) in kcal mol⁻¹, and entropy (S) in cal mol⁻¹ K⁻¹. Lowest vibrational wavenumber (ν) in cm⁻¹.

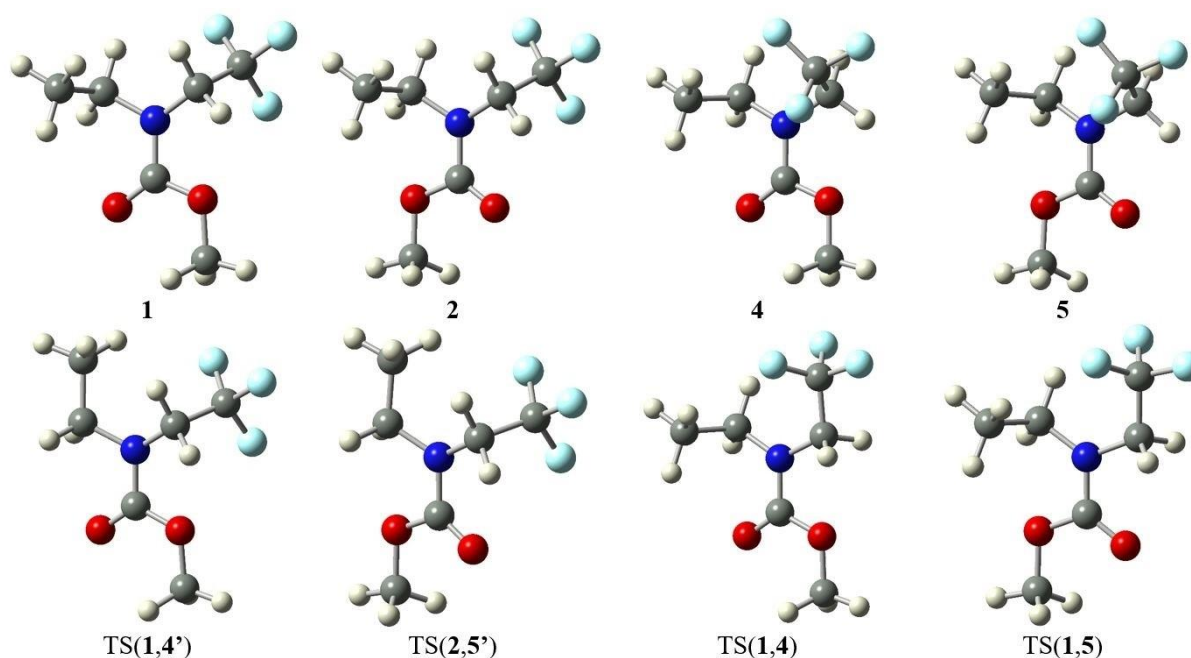


Figure 3. Optimized structures of the minima and alkyl rotation transition state structures of *N*-ethyl-*N*-(2,2,2-trifluoroethyl) methyl carbamate.

coordinates are provided in the Supporting Information. Higher level MPx energies are collected in Table S4 (gas phase) and Table S5 (SMD model, chloroform). Relative energies obtained with the SMD[MPx] and MPx data are included in Table 2 and Table S2, respectively.

The inclusion of solvent effects with the SMD model had only minor structural consequences as one might expect for solvents with low polarity and low dielectric constant ($\epsilon = 4.7113$). Therefore, we studied 1-dimensional rotational profiles and 2-dimensional rotation-inversion profiles without the SMD

Table 2. Relative energies and isomer populations computed at SMD[MP2] and higher-order SMD[MPx] levels.

Relative energies ^[a,b]	SMD[MP2]		SMD [MP3]		SMD[MP4]	
	ΔG_{rel}	ΔE_{rel}	(DQ)	(SDQ)	(SDTQ)	
E_{rel} , A vs. B	0.49	1.21	1.07	1.06	1.13	1.29
E_{rel} , C vs. B	0.75	1.11	0.98	1.02	1.10	1.23
A_{cr} (D)	15.04	14.17	14.11	13.86	13.68	13.47
A_{cr} (E)	15.39	14.79	14.61	14.32	14.20	14.12
A_{cr} (F)	21.72	20.87	25.53	25.14	25.04	25.16
E_{rel} , 1 vs. 2	0.20	0.31	0.25	0.26	0.27	0.31
E_{rel} , 4 vs. 2	0.56	0.79	0.73	0.74	0.73	0.72
E_{rel} , 5 vs. 2	0.49	0.58	0.58	0.58	0.55	0.52
E_{rel} , 1b vs. 1	1.66	1.26	1.41	1.41	1.33	1.15
E_{rel} , 2b vs. 2	1.99	1.73	1.83	1.86	1.79	1.66
A_{ar} (1,4')	4.87	3.86	3.77	3.79	3.78	3.70
A_{ar} (2,5')	4.80	3.93	3.86	3.90	3.86	3.75
A_{ar} (1,1a)	2.10	1.43	1.51	1.52	1.46	1.36
A_{ar} (1b,1a)	0.45	0.17	0.10	0.11	0.13	0.21
A_{ar} (2,2a)	2.35	1.86	1.87	1.91	1.88	1.84
A_{ar} (2b,2a)	0.36	0.13	0.04	0.06	0.09	0.18
A_{ar} (1,4)	7.64	6.34	6.33	6.36	6.31	6.17
A_{ar} (2,5)	7.47	6.41	6.28	6.32	6.33	6.28
1 to 2						
E_{rel} , 3a ₁ vs. 3b ₁	0.39	0.18	0.33	0.27	0.26	0.20
E_{rel} , 3a ₂ vs. 3b ₁	1.14	1.00	1.16	1.12	1.04	0.92
E_{rel} , 3b ₂ vs. 3b ₁	1.73	1.20	1.30	1.24	1.17	1.11
A_{cr} (1,3b ₁)	16.59	16.04	15.93	15.72	15.50	15.19
A_{cr} (2,3b ₁)	16.79	16.35	16.18	15.98	15.77	15.50
4 to 5						
E_{rel} , 6a ₁ vs. 6a ₂	6.36	6.46	6.24	6.29	6.25	6.30
E_{rel} , 6b ₁ vs. 6a ₂	5.80	5.85	5.70	5.75	5.69	5.69
E_{rel} , 6b ₂ vs. 6a ₂	0.65	0.48	0.43	0.40	0.45	0.52
A_{cr} (4,6a ₂)	13.05	12.53	12.65	12.33	12.12	11.83
A_{cr} (5,6a ₂)	13.13	12.73	12.80	12.50	12.30	12.02
Isomer populations ^[c]						
$p(1)$	0.28	0.27	0.28	0.28	0.27	0.26
$p(2)$	0.39	0.45	0.43	0.43	0.43	0.44
$p(4)$	0.15	0.12	0.13	0.12	0.13	0.13
$p(5)$	0.17	0.17	0.16	0.16	0.17	0.18
$p(1,4)$	0.44	0.38	0.41	0.40	0.40	0.39
$p(2,5)$	0.56	0.62	0.59	0.60	0.60	0.61

[a] All data computed with the 6–311++G(d,p) basis set and based on the SMD[MP2(fc)/6–311++G(d,p)] structures with scrf=(smd, solvent=chloroform). [b] Activation energies with respect to *N*-inversion (A_{inv}), *N*-alkyl rotation (A_{ar}), and carbamate rotation (A_{cr}), and relative isomers energies (E_{rel}) in terms of electronic energy (ΔE_{rel}) and Gibbs' free energy (ΔG_{rel}) in kcal mol⁻¹. [c] Boltzmann populations $p(n)$.

solvent system. However, all stationary structures were optimized using SMD[MP2].

NMR Computations

The GIAO method^[25,26] was employed to compute nuclear magnetic shielding for minima 1, 2, 4, and 5 of model VII. The shielding of tetramethylsilane (TMS) was also computed at the same level to determine chemical shifts. The C–F coupling constants were computed with the mixed spin-spin method.^[27] Several functionals were investigated including B3LYP^[28] and the HF mixed local density functionals BHandH [Eq. (1)] and BHandHLYP [Eq. (2)].^[29] Both the BHandH and BHandHLYP functionals includes contributions from the HF exchange functional, the local spin density approximation, and the correlation energy density functional by Lee, Yang, and Parr.^[30,31] BHandHLYP also incorporates contributions from Becke's 1988 func-

tional which includes Slater exchange and density gradient corrections.^[32]

$$\text{BHandH} : 0.5 \cdot E_{\text{X}}^{\text{HF}} + 0.5 \cdot E_{\text{X}}^{\text{LSDA}} + E_{\text{C}}^{\text{LYP}} \quad (1)$$

$$\text{BHandHLYP} : 0.5 \cdot E_{\text{X}}^{\text{HF}} + 0.5 \cdot E_{\text{X}}^{\text{LSDA}} + \Delta E_{\text{X}}^{\text{Becke88}} + E_{\text{C}}^{\text{LYP}} \quad (2)$$

A variety of basis sets were explored in the NMR computations including two variations of the 6–311G basis set; one with diffuse and expanded polarization functions applied to heavy atoms, 6–311+G(2d,p),^[17] and one with diffuse and expanded polarization functions on both heavy atoms and hydrogen, 6–311++G(3df,3pd).^[17] Augmented correlation consistent basis sets were also investigated including the triple- and quadruple-zeta basis sets aug-cc-pVTZ and aug-cc-pVQZ.^[33] A universal solvation model based on solute electron density (SMD) was also applied in the NMR calculations in an effort to reproduce the chloroform solution employed in the measurement of the ¹³C NMR spectra.

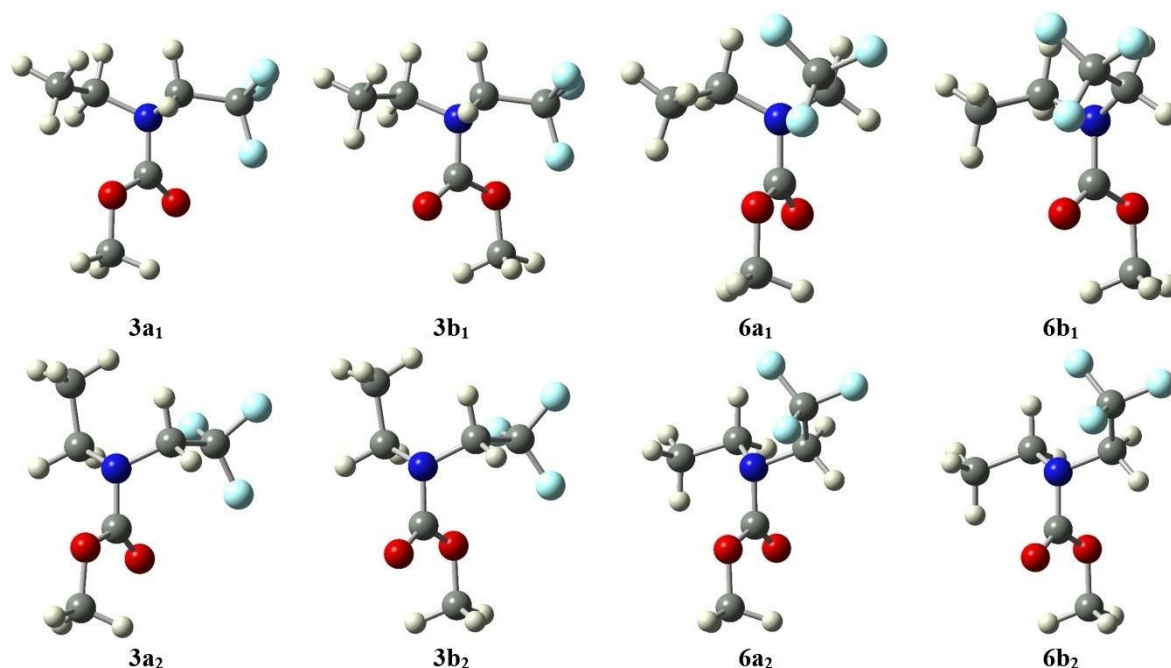


Figure 4. Optimized structures of the carbamate rotational transition state structures of *N*-ethyl-*N*-(2,2,2-trifluoroethyl) methyl carbamate.

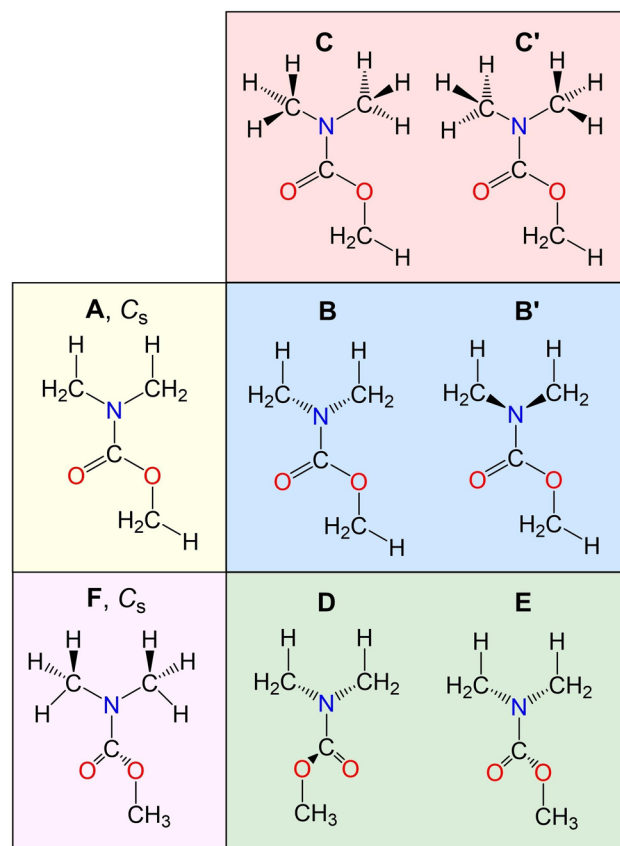
Results and Discussion

Potential Energy Surface Analysis of *N,N*-Dimethyl Methyl Carbamate

Lewis structures of *N,N*-dimethyl methyl carbamate are shown in Scheme 2, molecular models of the optimized structures **A–E** are shown in Figure 2 and energy data are collected in Tables 1 and 2. Table 3 lists dihedral angles that are pertinent to the discussion.

Based on simple concepts of resonance stabilization one might expect the C_s -symmetric structure **A** to be a minimum. Yet, we find **A** to be a second-order saddle point (SOSP) structure and the imaginary modes correspond to *N*-inversion ($i171.4\text{ cm}^{-1}$) and methyl rotations about the C–N bonds in opposite directions ($i80.4\text{ cm}^{-1}$). The minima are a pair of enantiomers **B** and **B'** with modest *N*-pyramidalization characterized by the improper dihedral angle $\pi = \angle(\text{H}_3\text{C}-\text{N}-\text{C}_{\text{carb}} \cdots \text{CH}_3) = 210.35^\circ$ where the first methyl is proximate to the carbamate methoxy group. At the level of optimization **B** is $\Delta G_{\text{rel}} = 0.49\text{ kcal/mol}$ preferred over **A**. Structures **A** and **B** adopt $\text{H}_3\text{C}-\text{N}$ bond conformations that place one hydrogen from each *N*-methyl group trans to the carbamate carbon. The degree of pyramidalization $\psi = |\pi - 180^\circ|$ is tabulated alongside improper dihedral π for each conformation to describe the absolute deviation from a planar state.

The conformations about the $\text{H}_3\text{C}-\text{N}$ bonds for structures **A–C** are described by dihedral angles α and β where $\alpha = \angle(\text{MeO}_2\text{C}-\text{N}-\text{CH}_2-\text{H}_{\text{CO}})$ refers to the methyl group on the carbonyl side, $\beta = \angle(\text{MeO}_2\text{C}-\text{N}-\text{CH}_2-\text{H}_{\text{COMe}})$ refers to the methyl group on the methoxy side, and both refer to the methyl hydrogen that is most trans to the carbamate carbon. In the C_s



Scheme 2. Lewis structures of the stationary structures of *N,N*-dimethyl methyl carbamate.

Table 3. Proper and improper dihedral angles (all in °) of the conformations of *N,N*-dimethyl methyl carbamate **VI** and *N*-ethyl-*N*-(2,2,2-trifluoroethyl) methyl carbamate **VII**.^[a-c]

Species	Proper dihedral ρ	Improper dihedral π	ψ	Proper dihedral α	Proper dihedral β
A	180.00	180.00	0.00	180.00	180.00
B	-164.17	210.35	30.35	159.11	-165.64
C	175.26	167.93	12.07	159.64	145.44
D	-60.67	238.67	58.67	175.70	-175.70
E	117.76	235.53	55.53	170.62	-170.62
F	88.89	177.77	2.23	~	~
				Proper Dihedral γ	Proper Dihedral δ
1	173.88	165.50	14.50	81.98	99.71
2	-7.82	160.37	19.63	77.81	102.27
4	-175.14	185.76	5.76	76.32	-99.86
5	5.65	187.17	7.17	77.81	-103.74
1a	-171.48	191.90	11.90	133.85	89.26
1b	-166.14	199.24	19.24	152.06	86.33
2a	3.72	186.15	6.15	129.42	97.00
2b	9.68	194.71	14.71	149.40	92.05
TS(1,4')	172.35	161.75	18.25	-177.33	94.41
TS(2,5')	-6.83	159.39	20.61	179.99	94.02
TS(1,4)	-176.41	185.72	5.72	80.97	-175.24
TS(2,5)	1.99	183.75	3.75	80.29	-173.18
3a₁	-100.75	132.83	47.17	83.13	70.83
3a₂	-64.49	222.12	42.12	169.64	72.25
3b₁	69.19	130.97	49.03	80.54	71.51
3b₂	118.71	219.83	39.83	169.69	71.75
6a₁	-101.85	152.27	27.73	58.20	-91.97
6a₂	-63.63	235.41	55.41	61.27	134.05
6b₁	77.81	151.92	28.08	54.58	-85.32
6b₂	117.24	233.10	53.10	56.02	-136.11

[a] All data based on the SMD[MP2(fc)/6-311++G(d,p)] structures with scrf=(smd, solvent=chloroform). [b] Degree of pyramidalization $\psi = |\pi - 180^\circ|$. [c] Proper dihedral angles $\alpha = \angle(\text{MeO}_2\text{C}-\text{N}-\text{CH}_2-\text{H}_{\text{CO}})$, $\beta = \angle(\text{MeO}_2\text{C}-\text{N}-\text{CH}_2-\text{H}_{\text{COMe}})$, $\gamma = \angle(\text{MeO}_2\text{C}-\text{N}-\text{CH}_2-\text{CH}_3)$, and $\delta = \angle(\text{MeO}_2\text{C}-\text{N}-\text{CH}_2-\text{CF}_3)$. For the parent system **A-E**, $\rho = \angle(\text{H}_3\text{C}-\text{N}-\text{C}(\text{OMe})=\text{O})$, $\pi = \angle(\text{H}_3\text{C}-\text{N}-\text{C}_{\text{carb}}\cdots\text{CH}_3)$. For the fluorinated model systems **VII** $\rho = \angle(\text{F}_3\text{C}_2\text{CH}_2\text{C}-\text{N}-\text{C}(\text{OMe})=\text{O})$, $\pi = \angle(\text{F}_3\text{C}_2\text{H}_2\text{C}-\text{N}-\text{C}_{\text{carb}}\cdots\text{CH}_2\text{CH}_3)$.

symmetric transition state structures **D** and **E** the methyl groups are symmetry related and the definition of α and β requires an additional rule to prioritize the methyl groups. The magnitude of the parameter π depends on the priorities of the two methyl groups and we chose to assign the priorities such that $\pi > 180^\circ$. Therefore, in Scheme 2 the methyl group in the upper right position has higher priority over the methyl group in the upper left position. The dihedral angle β is defined using the higher priority methyl group, and α is defined using the lower priority methyl group.

The rotation about the methyl *N*-bonds is essentially free with an activation barrier for *N*-alkyl rotation A_{ar} of $\Delta G_{\text{rel}} = 1.0$ kcal/mol, proceeds via transition state structures **C** ($\alpha = 159.6^\circ$; $\beta = 145.4^\circ$) and **C'** ($\alpha = -159.6^\circ$; $\beta = -145.4^\circ$) and is geared in that the methyl rotation about one $\text{H}_3\text{C}-\text{N}$ bond is accompanied by methyl rotation about the other $\text{H}_3\text{C}-\text{N}$ bond in the opposite direction. The rotations about the $\text{H}_3\text{C}-\text{N}$ bonds proceed with a reduction of the *N*-pyramidalization to $\pi(\text{C}) = 167.9^\circ$ in the rotational transition state structures **C** and **C'**.

The barrier to internal rotation about the $\text{Me}_2\text{N}-\text{CO}_2\text{Me}$ carbamate bond is more interesting because this rotation

disrupts the amide-type resonance, and it is characterized by the proper dihedral angle $\rho = \angle(\text{H}_3\text{C}-\text{N}-\text{C}(\text{OMe})=\text{O})$, where we define ρ with the *N*-methyl group that is on the same side as the carbamate methoxy group in structures **A-C** and the higher priority methyl group in **D** and **E**.

We located transition state structures **D** ($\rho = -60.7^\circ$) and **E** ($\rho = 117.8^\circ$) and it is notable that their ρ values deviate from 90° because the carbamate rotation proceeds with *N* pyramidalization; $\pi(\text{D}) = 238.7^\circ$ and $\pi(\text{E}) = 235.5^\circ$. The *N*-lone pair is on the same side as the methoxy group in **D** while it is next to the carbonyl group in **E**. At the level of optimization, there is a small preference for **D** over **E** and the lowest activation barrier A_{cr} for the carbamate rotation is $\Delta G_{\text{rel}} = 15.0$ kcal/mol. We will consider **F**, the second-order saddle point (SOSP) that separates **D** and **E**, in the neighboring interactions section (*vide infra*).

Table 2 lists the ΔG_{rel} and ΔE_{rel} values computed at SMD[MP2(fc)/6-311++G(d,p)] and allows comparison to the ΔE_{rel} values computed at the higher SMD[MPX] levels. As can be seen, the level of optimization provides an accurate approximation to the data obtained at our highest level SMD[MP4(SDTQ)]. The largest theoretical level dependency occurs for the activation barriers associated with carbamate rotation, and this is expected because the disruption of carbamate resonance is associated with substantial changes in the electronic structures.

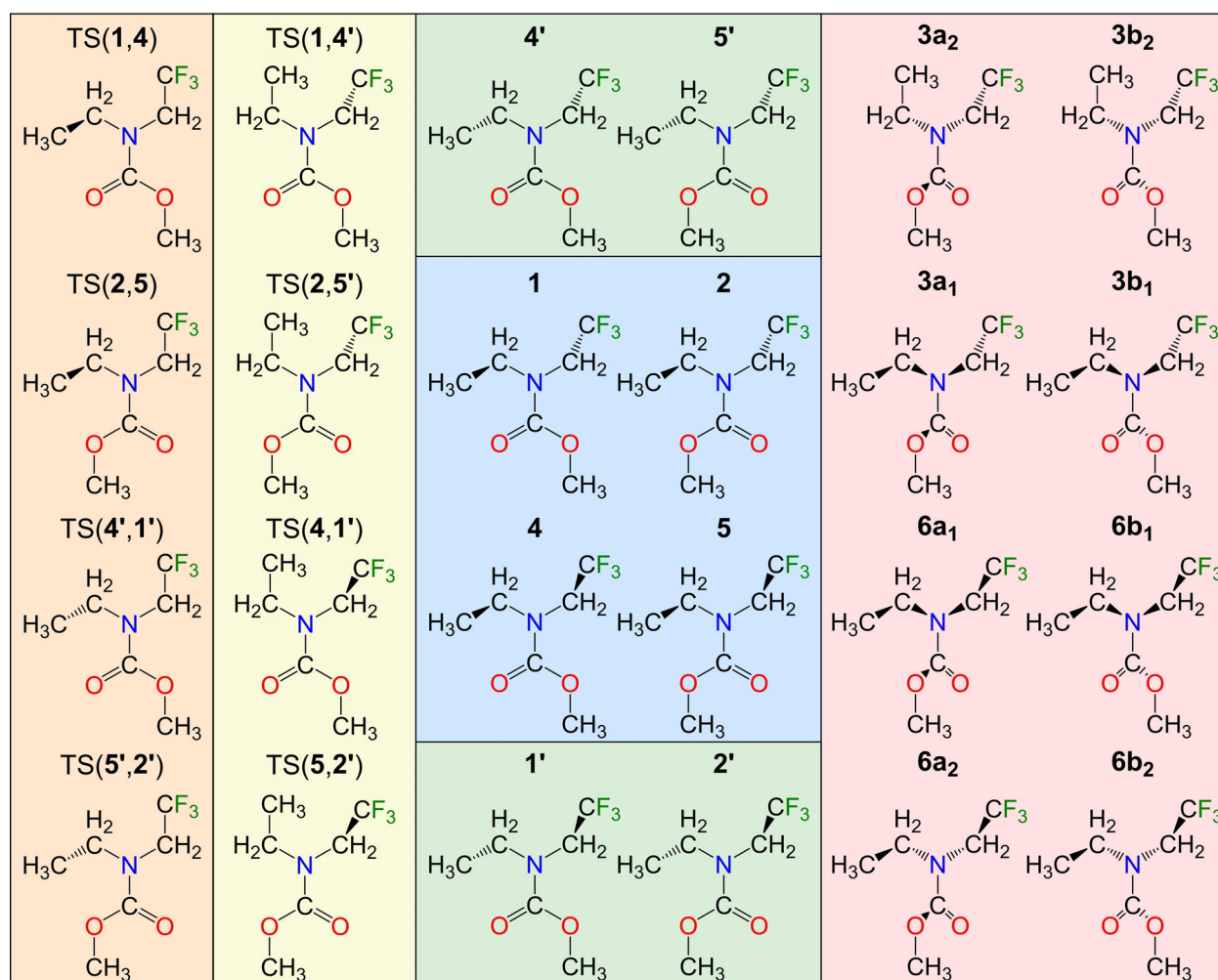
Potential Energy Surface Analysis of *N*-Ethyl-*N*-(2,2,2-Trifluoroethyl) Methyl Carbamate

Conformations

Lewis structures of *N*-ethyl-*N*-(2,2,2-trifluoroethyl) methyl carbamate **VII** are shown in Scheme 3, molecular models of the optimized structures are shown in Figures 3 and 4, energy data is included in Tables 1 and 2, and dihedral angles and degree of pyramidalization are collected in Table 3.

Each $\text{N}-\text{CH}_2$ bond allows for two possible conformations, the carbamate $\text{N}-\text{CO}_2\text{Me}$ bond allows for two rotamers, and therefore we expect eight stereoisomers and they come in four pairs of enantiomers. In the blue highlighted area of Scheme 3, we show four unique minima **1**, **2**, **4** and **5** which have in common that the conformation about the *N*-ethyl bond places the methyl group in proximity to one of the carbamate oxygens. In structures **1** and **2** the conformation about the *N*-trifluoroethyl group places the $-\text{CF}_3$ group on the *opposite* face and the carbamate rotation is accomplished via transition state structures **3**. In structures **4** and **5** the $-\text{CF}_3$ group is on the *same* face as the CH_3 group, and the carbamate rotation is accomplished via transition state structures **6**. For the forthcoming discussion of bond rotations and nitrogen inversions, it enhances clarity to include the drawings of **1'**, **2'**, **4'**, and **5'** in Scheme 3 to recognize these structures as the enantiomers of **1**, **2**, **4**, and **5**, respectively.

The conformations about the $\text{N}-\text{CO}_2\text{Me}$ bond are described by the proper dihedral $\rho = \angle(\text{F}_3\text{C}_2\text{CH}_2\text{C}-\text{N}-\text{C}(\text{OMe})=\text{O})$. The conformations about the $\text{H}_2\text{C}-\text{N}$ bonds are described by dihedral



Scheme 3. Lewis structures of stationary structures of *N*-ethyl-*N*-(2,2,2-trifluoroethyl) methyl carbamate. Minima (blue and green), ethyl C–N rotational transition state structures (yellow), trifluoroethyl C–N rotational transition state structures (orange), and carbamate rotational transition state structures (red).

angles γ and δ , where $\gamma = \angle(\text{MeO}_2\text{C}-\text{N}-\text{CH}_2-\text{CH}_3)$ and $\delta = \angle(\text{MeO}_2\text{C}-\text{N}-\text{CH}_2-\text{CF}_3)$. The pyramidal nitrogen is characterized by the improper dihedral angle $\pi = \angle(\text{F}_3\text{CH}_2\text{C}-\text{N}-\text{C}_{\text{carb}}-\text{CH}_2\text{CH}_3)$ and the derived parameter, $\psi = |\pi - 180^\circ|$, the degree of pyramidalization.

In structures **1** and **4** the carbamate carbonyl is on the opposite side relative to the fluorinated ethyl group with $|\rho| = 174.5 \pm 0.6^\circ$ (the *E*-rotamers), and in **2** and **5** it is on the same side with $|\rho| = 6.7 \pm 1.1^\circ$ (the *Z*-rotamers). There are several options for the conformations about the N–CH₂CH₃ and the N–CH₂CF₃ bonds. One might expect a trans conformation with respect to the –CO₂Me group for at least one of the two alkyl groups. However, we found that neither the CH₃ group nor the –CF₃ group are placed in such a trans position. Instead, both groups are placed above or below the best carbamate plane in clinal structures with dihedral angles $|\gamma| = 78.5 \pm 2.1^\circ$ and $|\delta| = 101.4 \pm 1.7^\circ$.

This scenario allows for two stereoisomers for each carbamate rotamer that come as pairs of enantiomers. We chose to show only the stereoisomers with positive γ dihedral

angles for minima **1**, **2**, **4**, and **5** in Figures 3 and 4. Structures **1** and **2** have the methyl and the –CF₃ groups on opposite sides of the carbamate plane (δ is positive), while those groups are on the same side in structures **4** and **5** (δ is negative).

Isomer *Z*-**2** is the most stable and the relative energies of *E*-**1**, *E*-**4**, and *Z*-**5** are listed in Table 2. *Z*-**2** is preferred over *Z*-**5** by $\Delta G_{\text{rel}} = 0.49$ kcal/mol and *E*-**1** is more stable than *E*-**4** by $\Delta G_{\text{rel}} = 0.48$ kcal/mol. The energy of *E*-**1** relative to *Z*-**2** is the *Z*-preference energy and is calculated to be $\Delta G_{\text{rel}} = 0.2$ kcal/mol at the level of optimization. Note that the theoretical level dependency of the total energy is very modest, and the relative energies ΔE_{rel} computed at the MP2 and full MP4 levels are usually less than 0.1 kcal/mol. At the bottom of Table 2, the Boltzmann populations are provided for the minima $p(\mathbf{n})$ and for the *E*- and *Z*-ensembles $p(\mathbf{n}, \mathbf{m})$. The *Z*-rotamers **2** and **5** have a combined population of $p(\mathbf{2}, \mathbf{5}) = 0.56$ and a small advantage over the combined *E*-population $p(\mathbf{1}, \mathbf{4}) = 0.44$.

Rotational Profiles about the N-Alkyl Bonds

The *N*-ethyl rotational profiles of **VII** were studied by scanning the proper dihedral angle γ (Figure 5). Rotation of the methyl group in **1** away from the carbamate function leads to **4'** as shown in Scheme 3 via transition state structure TS(1,4') with $\gamma = -177.3^\circ$ (Table 3). The analogous rotation of the methyl group in **2** leads to **5'** as shown via TS(2,5') with $\gamma = 179.9^\circ$. The activation barriers A_{ar} for these CN bond rotations are small as expected with $A_{ar}(1,4') = 4.9$ kcal/mol and $A_{ar}(2,5') = 4.8$ kcal/mol (Table 2).

An interesting feature of the rotational profiles is the appearance of shallow local minima **1b** at $\gamma \approx 152.1^\circ$ and **2b** at $\gamma \approx 149.4^\circ$. We optimized **1b** and **2b** as well as the adjacent minor barriers **1a** and **2a**, respectively, and their energies are included in Table 1. Both **1b** and **2b** do not qualify as stationary

minima because the height of the adjacent barriers is so low that the well does not support a bound vibrational state; $A_{ar}(1b,1a) = 0.45$ kcal/mol and $A_{ar}(2b,2a) = 0.36$ kcal/mol.

The *N*-trifluoroethyl rotational profile of **VII** was studied by scanning the proper dihedral angle δ (Figure 6). Rotation of the $-\text{CF}_3$ group in **1** through the carbamate plane leads to minimum **4** as shown in Scheme 3 via transition state structure TS(1,4) with $\delta = -175.2^\circ$. By analogy, rotation of the $-\text{CF}_3$ group in **2** around the $\text{N}-\text{CH}_2\text{CF}_3$ leads to **5** via TS(2,5) with $\delta = -173.2^\circ$. The activation barriers $A_{ar}(1,4) = 6.34$ kcal/mol and $A_{ar}(2,5) = 6.41$ kcal/mol are slightly larger than the γ rotational profiles.

We recognize that TS(1,4) is the enantiomer of the transition state structure for the enantiomeric process of **1'** to **4'**, $\text{TS}(1,4) = \text{TS}'(1',4')$, and by analogy $\text{TS}(2,5) = \text{TS}'(2',5')$. Enantiomerization

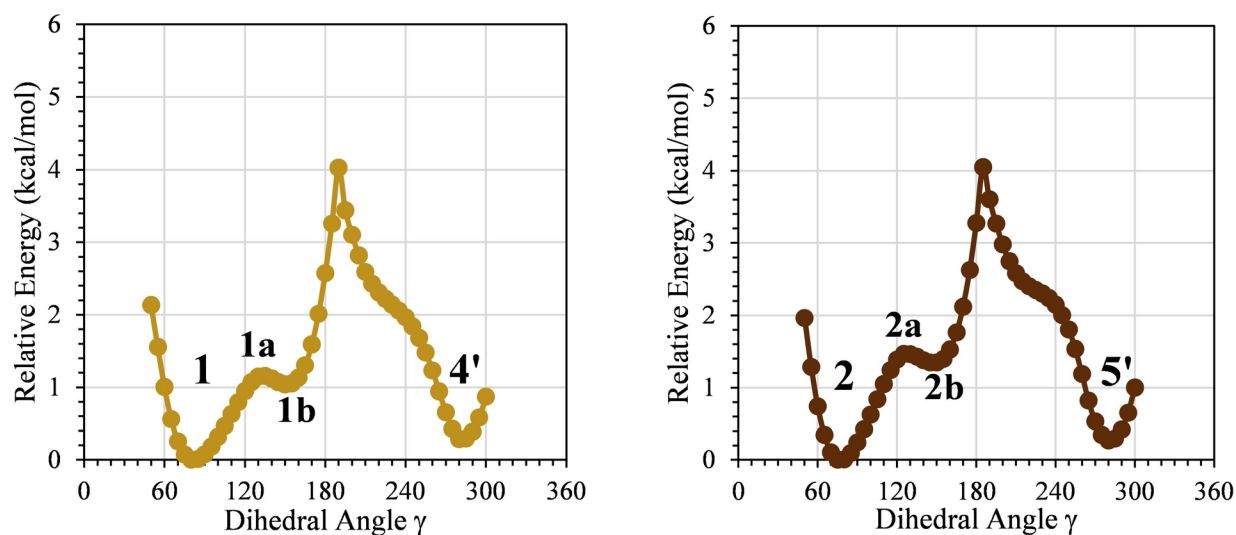


Figure 5. *N*-alkyl rotational profiles about the Et-N bond as a function of dihedral angle γ of **1** to **4'** (left, yellow circles) and **2** to **5'** (right, brown circles).

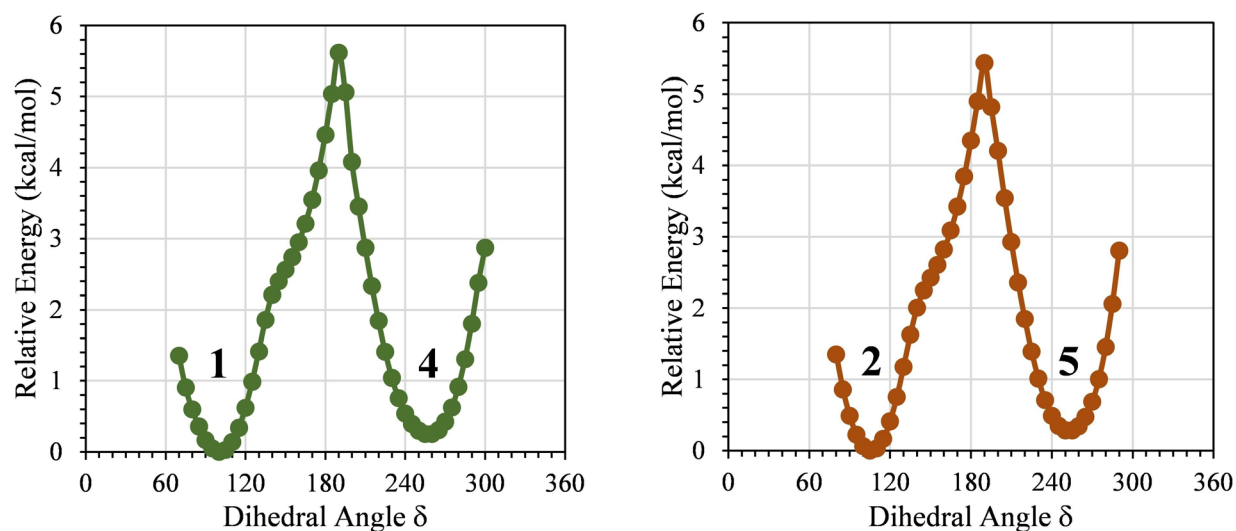


Figure 6. *N*-alkyl rotational profiles about the $\text{F}_3\text{CH}_2\text{C}-\text{N}$ bond as a function of dihedral angle δ of **1** to **4** (left, green circles) and **2** to **5** (right, orange circles).

of any one minimum requires a two-step process. For example, the enantiomerization of **1** to **1'** can be accomplished either via **1** \rightarrow $-\text{[TS(1,4)]}$ \rightarrow **4'** \rightarrow $-\text{[TS(1',4')]}$ \rightarrow **1'** where $-\text{CH}_3$ rotation precedes $-\text{CF}_3$ rotation or by the sequence **1** \rightarrow $-\text{[TS(1,4)]}$ \rightarrow **4** \rightarrow $-\text{[TS(1',4)]}$ \rightarrow **1'** where $-\text{CF}_3$ rotation precedes $-\text{CH}_3$ rotation. The ensembles of stereoisomers $\{1, 4\}$ and $\{2, 5\}$ interconvert and enantiomerize fast, and interconversion between any members of these ensembles requires carbamate rotation.

Rotational Profiles about the Carbamate $\text{CF}_3\text{CH}_2\text{-N(Et)-C(OMe)=O}$ Bond and Rotation-Inversion Surface Analysis

The CN carbamate rotational profiles of **VII** were studied by scanning the proper dihedral angle ρ (Figure 7) with surprising outcomes. Our first approach aimed to generate the relaxed ρ scans driving ρ from structure **2** to **1** in different directions and we obtained transition state structures **3a₁**, by reducing ρ and **3a₂**, by increasing ρ . We then drove ρ from **1** to **2** and again in different directions and obtained two more transition state structures: reducing ρ led to **3b₁** and increasing ρ led to **3b₂**. The same situations occurred by scanning from **4** to **5** and from **5** to **4** and resulted in four more transition state structures **6**. In all cases, the relaxed scans collapsed shortly after reaching any of the transition state structures **3** or **6**. The discontinuities in the standard relaxed scans are a consequence of the correlation between carbamate bond rotation and the *N*-pyramidalization. We will model continuous path for carbamate rotation on 2-dimensional $E(\rho, \pi)$ surfaces (*vide infra*). However, even based on the information obtained from the 1-dimensional $E(\rho)$ scans shown in Figure 7, it is apparent which rotational transition state structure is the lowest in each ensemble.

There are eight transition state structures for carbamate rotation (Scheme 3) because there are two isomerization reactions **1** \rightleftharpoons **2** via **3** and **4** \rightleftharpoons **5** via **6** and each one of these

reactions can be realized with carbamate bond rotations ρ in two directions (**a** or **b**) and two directions for *N* pyramidalization π (subscripts **1** or **2**). It was found that **3b₁** is the preferred transition state structure for the isomerization **1** \rightleftharpoons **2**, and that the path via **6a₂** is preferred for the process **4** \rightleftharpoons **5**.

To model continuous paths for carbamate rotation it became necessary to build 2-dimensional $E(\rho, \pi)$ surfaces that show the potential energy as a function of both carbamate rotation ρ and *N*-pyramidalization π . We generated two surfaces $E(\rho, \pi)$ for each isomerization **1** \rightleftharpoons **2** and **4** \rightleftharpoons **5** by compiling large numbers of π scans for discrete ρ values. The surfaces that show the transition state structures **3b** and **6a** are shown in Figure 8, and the other two surfaces with the transition state structures **3a** and **6b** are provided in Figure S1.

The activation energy from each minimum to each adjacent transition state was calculated at the level of optimization, SMD[MP2] and higher-order SMD[MPx/MP2] levels. The average variance between the SMD[MP2] energy and the highest SMD[MP4(SDTQ)/MP2] energies is only $\Delta\Delta E \approx 0.78$ kcal/mol (Table 2), demonstrating that SMD[MP2] adequately describes the activation energies in our carbamate rotational profiles.

$$A_{\text{rot}}(\text{VII}) = F_2 \sum F_{3i}^* A_{\text{cr}}(2, 3i) + F_5 \sum F_{6i}^* A_{\text{cr}}(5, 6i) \quad (3)$$

$$F_{3i} = \frac{p_{3i}}{\sum p_{3i}} = e^{-\frac{E_{3i}}{RT}} / \sum e^{-\frac{E_{3i}}{RT}} \quad (4)$$

$$F_{6i} = \frac{p_{6i}}{\sum p_{6i}} = e^{-\frac{E_{6i}}{RT}} / \sum e^{-\frac{E_{6i}}{RT}} \quad (5)$$

$$F_2 = \frac{p_2}{p_2 + p_5} = e^{-\frac{E_2}{RT}} / (e^{-\frac{E_2}{RT}} + e^{-\frac{E_5}{RT}}) \quad (6)$$

$$F_5 = \frac{p_5}{p_2 + p_5} = e^{-\frac{E_5}{RT}} / (e^{-\frac{E_2}{RT}} + e^{-\frac{E_5}{RT}}) \quad (7)$$

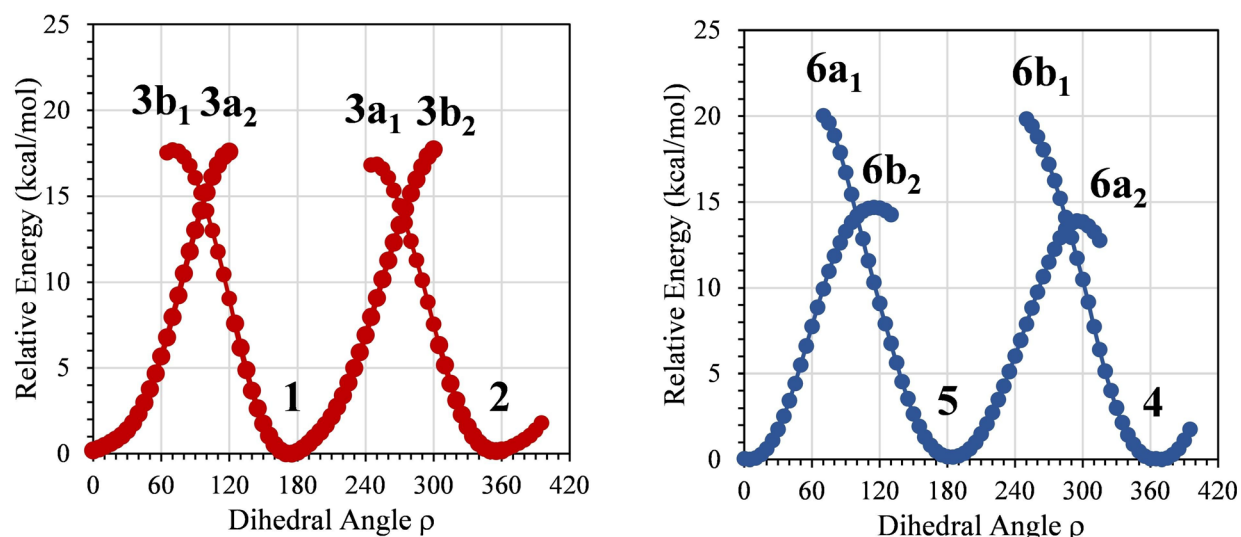


Figure 7. Carbamate rotational profiles from **1** to **2** (red circles) with **3b** surface plot, and from **4** to **5** (blue circles) with **6a** surface plot.

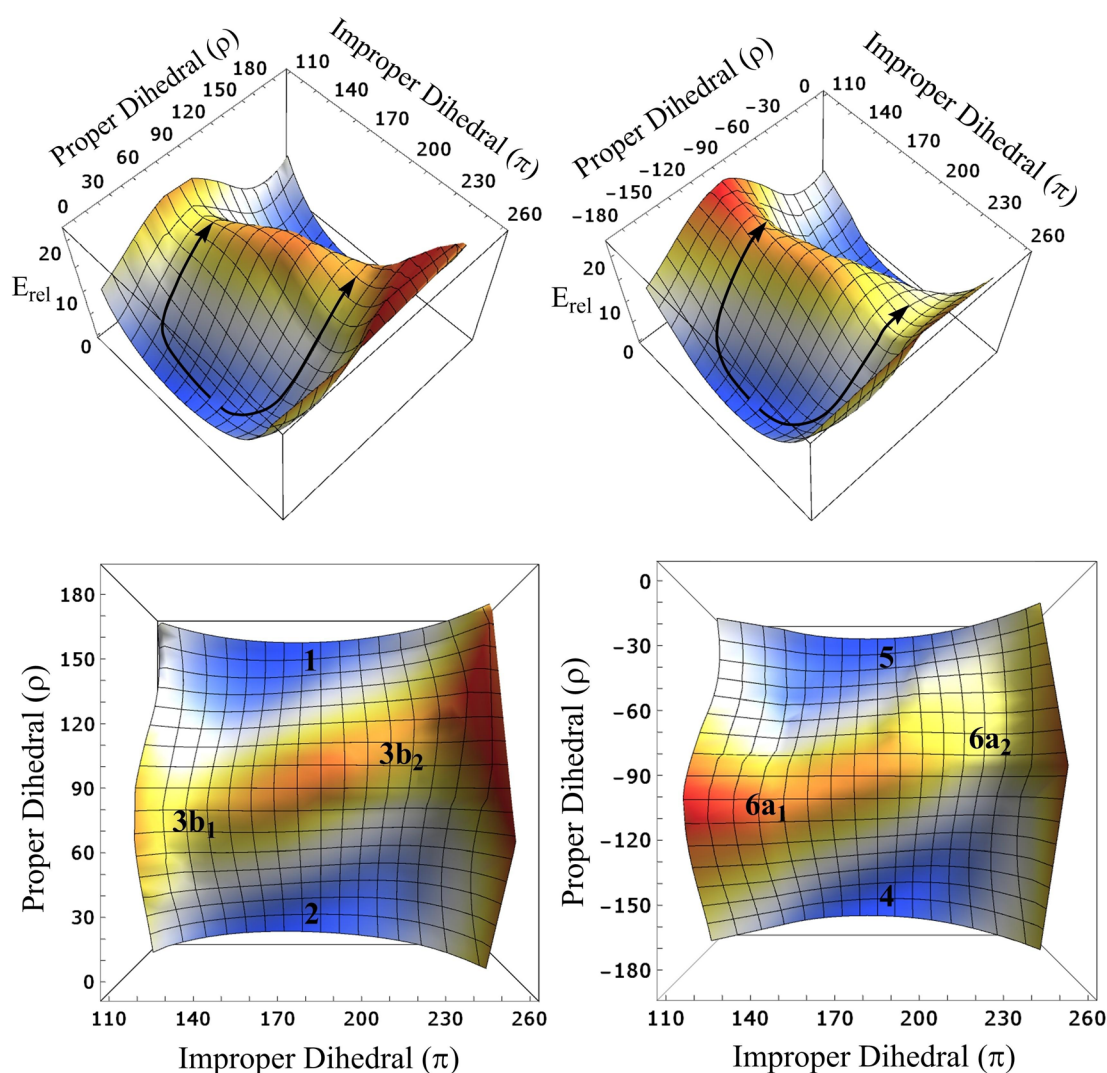


Figure 8. Rotation-inversion surfaces $E(\rho, \pi)$ for E/Z -isomerizations $E-1 \rightleftharpoons Z-2$ (left) via TS structures **3b** and $E-4 \rightleftharpoons Z-5$ (right) TS structures **6a**.

The measured overall activation barrier $A_{\text{rot}}(\text{VII})$ for E/Z isomerizations $1 \rightleftharpoons 2$ and $4 \rightleftharpoons 5$ depends on the probabilities of eight isomerization pathways and is determined via Equation (3). Equation (3) assumes that the CN-rotations (ca. 100 cm^{-1} in minima, ca. 1100 cm^{-1} in TS structures) and the N -inversions (ca. 230 cm^{-1}) are independent which appears justified based on the separation of their vibrational frequencies. The relative probability for a path via a transition state structure **3i** ($i = a_1, a_2, b_1, b_2$) with activation barrier $A_{\text{cr}}(\mathbf{2,3i})$ is weighted by the partition function F_{3i} which depends on the Boltzmann populations p_{3i} [Eq. (4)]. In analogy, the relative probability for a path via a transition state structure **6i** with $A_{\text{cr}}(\mathbf{5,6i})$ is weighted by the partition function F_{6i} [Eq. (5)]. The factors F_2 and F_5 account for the Boltzmann populations of **2** and **5** [Eqs. (6) and (7)]. Equations (3)–(7) were evaluated using Gibbs's free energies G_{298} calculated at SMD[MP2(fc)/6-311++G(d,p)] and reported in Table 1 and result in our final computational estimate of the overall rotation-inversion barrier $A_{\text{rot}}(\text{VII}) = 15.90 \text{ kcal/mol}$.

It is a major conceptual advance to discuss *multi-paths* scenarios as compared to the simple scenario involving just one pair of TS structures. Because of the presence of the ethyl and trifluoroethyl groups, our *multi-paths* scenario involves four pairs of TS structures; see the pairs **3a₂/3b₂**, **3a₁/3b₁**, **6a₁/6b₁**, and **6a₂/6b₂** in our manuscript (Scheme 3). The very point is that the reductionist approach fails; that is, the analysis of a basic model system (such as **VI**) does not inform in a sufficient manner about more complicated systems (such as **VII**). The effects of longer chain N -alkyl substitution and/or fluorination greatly affects the number of stable minima and TS structures, and by extension the overall rotational barrier.

In related experimental studies,^[34] the rotational barrier of carbamate **II** (Figure 1) was determined by variable temperature ^{13}C and ^{19}F NMR measurements. The analysis using the modified Eyring equation^[35,36] resulted in the rotational energy barrier of $A_{\text{exp}}(\text{II}) = 15.93 \pm 0.59 \text{ kcal/mol}$, in close agreement with the computed estimate of $A_{\text{rot}}(\text{VII})$. Rotational barriers were also determined experimentally for similar N,N -dialkyl O -alkyl carba-

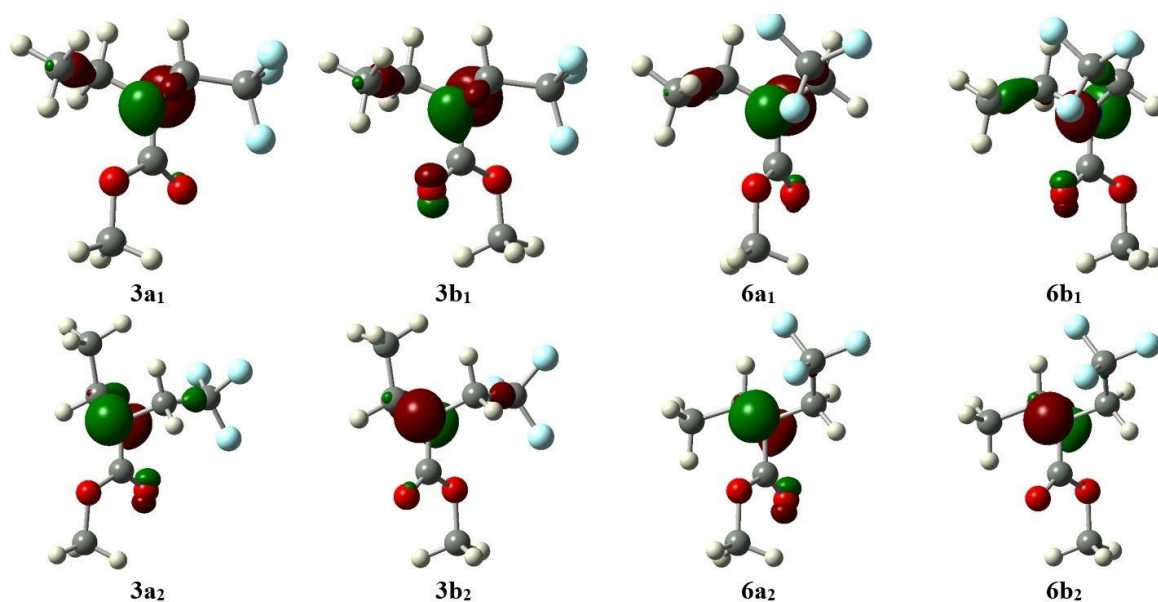


Figure 10. Highest occupied molecular orbital (HOMO) of transition state structures 3 and 6.

tion is enhanced by pyramidalization of the carbamate's *N*-lone pair because it concentrates *N*-lone pair electron density on the backside of the carbamate CO bonds. A similar effect was observed by Kost et al. in which they studied the effect of substituent electronegativity on $NLP \rightarrow \sigma^*$ donation in sulfenamides.^[39]

The highest occupied molecular orbitals (HOMO) were analyzed for transition state structures 3 and 6 to compare the extent of $NLP \rightarrow \sigma^*$ donation and the results are shown in Figure 10. The results provide compelling evidence that the TS structures strongly engage in $NLP \rightarrow \sigma^*(C=O)$ donation but only weakly in $NLP \rightarrow \sigma^*(C-OMe)$ donation. Therefore $NLP \rightarrow \sigma^*(C=O)$ donation, in conjunction with the observed NLP/CO_2 repulsion, is responsible for a considerable amount of stabilization (ca. 2.6 kcal/mol) in the two most stable transition state structures in each ensemble, **3a₂/3b₁** and **6b₁/6a₂**.

Incipient Nucleophilic Attack and $CH \cdots$ Cation Contacts

Electrostatic stabilization is realized by placing the electron density of one fluorine atom of the CF_3 group in proximity to the positively charged carbamate-C. This interaction could be described as an incipient nucleophilic attack^[40] because *F*-lone pair density is oriented towards the electrophilic carbamate-C. Through-space halogen \cdots carbonyl-C interactions are well precedented.^[41] The term incipient nucleophilic attack might imply the notion of electron density transfer, i.e., halogen \rightarrow carbonyl-C. However, the important feature is the placement of electron density close to a positively charged center and the resulting Coulombic stabilization and polarization of that electron density in the electric field of the electrophilic center. From this perspective, one realizes that a similar stabilization can be achieved by placing one H atom of the CH_3 group of the

N-ethyl group in proximity to the positively charged carbamate-C. Interactions of this type may be called $CH \cdots$ cation contacts and they are common in crystallography.^[42]

In structures **3a₂/3b₁**, the proximate fluorine F_p of the CF_3 group is placed close to the positively charged carbamate-C, and in **6b₁/6a₂**, the proximate methyl hydrogen H_p is positioned close to the carbamate-C. These stabilizing interactions are characterized by an elongation of the corresponding X_2C-X_p covalent bond ($X=H, F$) and a reduction of the through-space $X_p \cdots C=O$ distance (Table 5). This intrinsic structural feature is affected very little by the application of the SMD solvent system (Table S6).

Coulombic stabilization and $NLP \rightarrow \sigma^*$ donation were correlated with the overall energy of all eight transition state structures to compare the net effect of each stabilizing factor (Scheme 4). It was found that structures that engage in $NLP \rightarrow \sigma^*(C=O)$ negative hyperconjugation and $X_p \cdots C=O$ contact were the most stable, **3b₁/6a₂** (blue), and that structures that had neither were the least stable, **3b₂/6a₁** (red). Between these two extremes there are two possible combinations of $X_p \cdots C=O$ contact and $NLP \rightarrow \sigma^*$ hyperconjugation to either CO bond. It

Table 5. Through-space coulombic stabilization of TS Structures 3 and 6.^[a]

Stability	TS Str.	E_{rel}	X_p	$X_p \cdots C=O$	$C-X_p$
2	3a₁	0.39	F	2.911	1.348
3	3a₂	1.14	F	3.197	1.345
1	3b₁	0.00	F	2.875	1.349
4	3b₂	1.73	F	3.344	1.341
4	6a₁	6.36	H	2.921	1.092
1	6a₂	0.00	H	2.616	1.095
3	6b₁	5.80	H	2.830	1.093
2	6b₂	0.65	H	2.608	1.095

[a] Relative energies (E_{rel}) based on the SMD[MP2/6-311++G(d,p)] energies with scrf=(smd, solvent=chloroform) in kcal mol⁻¹.

w/o $X_p \cdots C=O$	3a₂, 6b₁	3b₂, 6a₁
w/ $X_p \cdots C=O$	3b₁, 6a₂	3a₁, 6b₂
	$NLP \rightarrow \sigma^*(C=O)$	$NLP \rightarrow \sigma^*(C-OMe)$

Scheme 4. Correlation of TS-stability of **3** and **6** with $NLP \rightarrow \sigma^*$ and $X_p \cdots C=O$ donation.

was determined that $X_p \cdots C=O$ contact was the deciding factor, where structures **3a₁/6b₂** were the second most stable, and **3a₂/6b₁** were the third most stable.

Our discussion of the neighboring group interactions presents a significant conceptual advance. The idea of NLP/CO_2 repulsion minimization is original. There have been no previous discussions involving the synergetic interplay between NLP/CO_2 repulsion minimization and $NLP \rightarrow \sigma^*(CO)$ negative hyperconjugation. And of course, the need for the discussion we present in section "Incipient Nucleophilic Attack and $CH \cdots$ Cation Contacts" is a direct consequence of the progression from a reductionist model system to a more realistic, larger system.

Computed ^{13}C NMR Chemical Shifts and $J(^{13}C, ^{19}F)$ Coupling Constants

Experimentally measured chemical shifts $\delta(^{13}C)$ and coupling constants $J(^{13}C, ^{19}F)$ for the three synthesized compounds **II**, **III**, and **IV** are listed at the top of Table 6. The chemical shifts are provided for the centers of left and right quartets, i.e., the quartets with the higher and lower chemical shifts, along with the offset $\Delta\delta$ between the two sets. In analogy, we report the J

values measured for the left and right signals and their difference ΔJ . Note that compound **II** mostly closely resembles the computed model system **VII**.

The chemical shifts $\delta(^{13}C)$ and the coupling constants $J(^{13}C, ^{19}F)$ were calculated for model system **VII** using a range of functionals and basis sets (Table 6). The data computed for E -rotamers {**1**, **4**} and Z -rotamers {**2**, **5**} were averaged in each ensemble; these averages are listed in Table 6 and they correspond to the measured signals observed in the experimental ^{13}C NMR. The coupling constants $J(^{13}C, ^{19}F)$ listed are averaged over the three C–F bonds and over the rotamers in each ensemble. The non-averaged NMR data computed with each method are provided in Table S2. The SMD model was employed to include the effects of bulk solvation in chloroform because the NMR spectra were recorded in deuterated chloroform. In Table 6 we report both the NMR data without and with solvation in successive rows, respectively.

We initially employed the most commonly used hybrid density functional B3LYP and found the chemical shifts to be overestimated by roughly 10% and the magnitude of the J -values by about 25%. The $\Delta\delta$ and ΔJ values are of the correct order of magnitude. There is a small basis set dependency but improvements in the basis set trends in the wrong direction. Keller and Szczecinski^[43] reported that the hybrid functionals BHandH and BHandHLYP performed more effectively in GIAO calculations for fluorine-containing compounds. Indeed, these density functionals afford chemical shifts $\delta(^{13}C)$ within 6% of the experimental data and coupling constants $J(^{13}C, ^{19}F)$ that also are within 6% of measured data. In all theoretical models, the inclusion of chloroform solvation seemingly increased the accuracy of the offset $\Delta\delta$ and of ΔJ between ensembles {**1**, **4**} and {**2**, **5**} but absolute chemical shifts $\delta(^{13}C)$ may not.

Table 6. Computational and experimental ^{13}C - ^{19}F NMR data.^[a–c]

Experimental	$\delta(^{13}C)$ [ppm]		$\Delta\delta$ [ppm]	$J(^{13}C, ^{19}F)$ [Hz]		ΔJ [Hz]
	Left signal	Right signal		Left signal	Right signal	
<i>N</i> ^ε -Boc- <i>N</i> ^ε -(2,2,2-trifluoroethyl)- <i>L</i> -lysinate (IV)	124.86	124.61	0.25	283.18	284.00	0.82
4-bromo- <i>N</i> -Boc- <i>N</i> -(2,2,2-trifluoroethyl)-butan-1-amine (III)	124.91	124.70	0.21	283.82	284.42	0.61
4-(Boc(2,2,2-trifluoroethyl)amino)-butan-1-ol (II)	124.81	123.62	0.20	283.19	282.59	0.60
Method	{ 1 , 4 }	{ 2 , 5 }		{ 1 , 4 }	{ 2 , 5 }	
B3LYP/6–311 + G(2d,p)	135.45	135.11	0.34	–355.32	–356.03	0.70
B3LYP/6–311 + G(2d,p) Solv.	137.14	136.81	0.33	–354.93	–355.78	0.85
B3LYP/aug-cc-pVTZ	137.10	136.78	0.32	–354.38	–355.06	0.68
B3LYP/aug-cc-pVTZ Solv.	138.79	138.49	0.30	–353.95	–354.78	0.83
B3LYP/aug-cc-pVQZ	139.52	139.20	0.32	–358.72	–359.41	0.69
B3LYP/aug-cc-pVQZ Solv.	141.27	140.97	0.31	–358.27	–359.11	0.84
BHandH/6–311 + + G(3df,3pd)	132.85	132.52	0.33	–295.81	–296.36	0.55
BHandH/6–311 + + G(3df,3pd) Solv.	134.71	134.39	0.32	–294.99	–295.68	0.69
BHandH/aug-cc-pVTZ	132.99	132.67	0.31	–297.69	–298.23	0.54
BHandH/aug-cc-pVTZ Solv.	132.69	132.39	0.30	–296.88	–297.56	0.68
BHandHLYP/6–311 + + G(3df,3pd)	130.37	130.05	0.32	–300.02	–300.63	0.61
BHandHLYP/6–311 + + G(3df,3pd) Solv.	132.13	131.82	0.31	–298.9	–299.65	0.75
BHandHLYP/aug-cc-pVTZ	130.59	130.29	0.30	–301.94	–302.53	0.59
BHandHLYP/aug-cc-pVTZ Solv.	132.31	132.02	0.29	–300.83	–301.57	0.74
BHandHLYP/aug-cc-pVQZ	132.52	132.21	0.30	–305.32	–305.95	0.63
BHandHLYP/aug-cc-pVQZ Solv.	134.29	133.99	0.30	–304.18	–304.92	0.74

[a] all job-types: nmr = (giao,spinspin,mixed). [b] Solv: scrf = (smd,solvent = chloroform). [c] All NMR calculated at 298 K.

Conclusions

The four unique asymmetric minima of model system **VII** differ by the orientations of the sidechain fluoroalkyl group (characterized by dihedral angle δ) and its position relative to the carbamate carbonyl-O (characterized by dihedral angle ρ). The *N*-alkyl conformers **1** and **4** are *E*-rotamers ($\rho \approx 180^\circ$) and the *N*-alkyl conformers **2** and **5** are *Z*-rotamers ($\rho \approx 0^\circ$). *N*-alkyl rotation is facile and allows minima within each ensemble (*E*-rotamers **1**, **4**, **1'**, **4'**; *Z*-rotamers **2**, **5**, **2'**, **5'**) to interconvert and enantio-merize fast. The *E*- and *Z*-ensembles are energetically similar with Boltzmann populations of $p(\mathbf{1,4}) = 0.44$ and $p(\mathbf{2,5}) = 0.56$.

We analyzed the rotational profiles about dihedral angle ρ to determine the barriers to the isomerizations *E*-**1** \rightleftharpoons *Z*-**2** via transition state structures **3** and the isomerizations *E*-**4** \rightleftharpoons *Z*-**5** via transition state structures **6**. Each *E/Z*-isomerization reaction is associated with four transition state structures depending on the mode of carbamate bond rotation (**a** or **b**) and the direction of the concomitant *N*-pyramidalization π (subscripts **1** or **2**). Of the eight transition state structures, the lowest energy paths proceed via **3b**₁ and **6a**₂. We have provided evidence from structural and MO analyses to argue that these transition state structures benefit from synergetic NLP/CO₂ repulsion minimization and NLP $\rightarrow \sigma^*(\text{CO})$ negative hyperconjugation, as well as X_p-C=O electrostatic stabilization.

The experimentally measured carbamate rotational barrier $A_{\text{rot}}(\mathbf{VII})$ is a composite of a number of isomerization reactions *E*-**1** \rightleftharpoons *Z*-**2** and *E*-**4** \rightleftharpoons *Z*-**5** along eight pathways via transition state structures **3i** and **6i** ($i = a_1, a_2, b_1, b_2$). The relative weights of the paths depend on the relative populations F_2 and F_5 of minima **2** and **5** and on relative stabilities F_{3i} and F_{6i} of the transition state structures. Our computational estimate of the overall rotation-inversion barrier was determined to be $A_{\text{rot}}(\mathbf{VII}) = 15.9$ kcal/mol. This value is in complete agreement with the measured rotational barrier of the structurally similar carbamate ester **II**, $A_{\text{exp}}(\mathbf{II}) = 15.9 \pm 0.6$,^[32] which was experimentally determined with variable-temperature ¹³C NMR spectroscopy.

To provide a direct link between theory and experiment, the results of the potential energy surface analysis were connected to the experimentally measured chemical shifts $\delta(^{13}\text{C})$ and $J(^{13}\text{C}, ^{19}\text{F})$ coupling constants. We computed the NMR chemical shift $\delta(^{13}\text{C})$ and $J(^{13}\text{C}, ^{19}\text{F})$ coupling constants of the stable minima **{1,4}** and **{2,5}** of model system **VII** using a variety of combinations of density functionals and basis sets. The hybrid functionals BHandH and BHandHLYP, developed by Keller and Szczecinski,^[42] performed most effectively in our GIAO calculations. The computation of chemical shifts $\delta(^{13}\text{C})$ and $J(^{13}\text{C}, ^{19}\text{F})$ coupling constants for the minima at our best theoretical levels and their Boltzmann averaging over **{1,4}** and **{2,5}** results in good agreement with the experimental NMR data (within 6%).

Supporting Information Summary

One figure showing the rotation-inversion surfaces $E(\rho, \pi)$ for *E/Z*-isomerizations *E*-**1** \rightleftharpoons *Z*-**2** via TS structures **3a** and *E*-**4** \rightleftharpoons *Z*-**5** TS

structures **6b**. Four tables documenting total and relative energies computed at various levels, and two tables providing structural information. One table listing the computed NMR data for model system **VII**. Cartesian coordinates of stationary structures **A–F** of *N,N*-dimethyl methyl carbamate and of stationary structures of all minima and transition state structures associated with 1–6 of *N*-ethyl-*N*-(2,2,2-trifluoroethyl) methyl carbamate determined at the MP2/6–311++G(d,p) level with SMD solvation.

Acknowledgements

The high-performance compute cluster was purchased in part with MRI funding by the National Science Foundation under Grant No. OAC-1919789.

Conflict of Interest

The authors declare no conflict of interest.

Data Availability Statement

The data that support the findings of this study are available in the supplementary material of this article.

Keywords: carbamates · multipaths equilibria · negative hyperconjugation · rotation-inversion · second-order saddle points

- [1] C. Dugave, L. Demange, *Chem. Rev.* **2003**, *103*, 2475–2532.
- [2] V. Krishnan, S. Vazquez, K. Maitra, S. Maitra, *Chem. Phys. Lett.* **2017**, *689*, 148–151.
- [3] G. Meng, S. Shi, R. Lalancette, R. Szostak, M. Szotak, *J. Am. Chem. Soc.* **2018**, *140*, 727–734.
- [4] K. Wiberg, *J. Org. Chem.* **2019**, *84*, 10938–10945.
- [5] R. Szostak, C. Liu, R. Lalancette, M. Szostak, *J. Org. Chem.* **2018**, *83*, 14676–14682.
- [6] P. Stilbs, S. Forsen, *J. Phys. Chem.* **1971**, *75*, 1901–1902.
- [7] V. Bryantsev, T. Firman, B. Hay, *J. Phys. Chem. A* **2005**, *109*, 832–842.
- [8] C. Cox, T. Lectka, *J. Org. Chem.* **1998**, *63*, 2426–2427.
- [9] M. Deetz, C. Forbes, M. Jonas, J. Malerich, B. Smith, O. Wiest, *J. Org. Chem.* **2002**, *67*, 3949–3952.
- [10] A. L. Moraczewski, L. A. Banaszynski, A. M. From, C. A. White, B. D. Smith, *J. Org. Chem.* **1998**, *63*, 7258–7262.
- [11] R. Pontes, E. Basso, F. Santos, *J. Org. Chem.* **2007**, *72*, 1901–1911.
- [12] E. N. Prabhakaran, S. Tumminakatti, K. Vats, S. Ghosh, *RSC Adv.* **2020**, *10*, 11871–11875.
- [13] N. Schädel, J. Gebhardt, M. Löffler, D. Garnier, N. Hansen, S. Laschat, *J. Phys. Org. Chem.* **2019**, *32*, 0894–3230.
- [14] G. Cavallo, P. Metrangolo, R. Milani, T. Pilati, A. Priimagi, G. Resnati, G. Terraneo, *Chem. Rev.* **2016**, *116*, 2478–2601.
- [15] *Gaussian 16, Revision C.01*, M. J. Frisch, G. W. Trucks, H. B. Schlegel, G. E. Scuseria, M. A. Robb, J. R. Cheeseman, G. Scalmani, V. Barone, G. A. Petersson, H. Nakatsuji, X. Li, M. Caricato, A. V. Marenich, J. Bloino, B. G. Janesko, R. Gomperts, B. Mennucci, H. P. Hratchian, J. V. Ortiz, A. F. Izmaylov, J. L. Sonnenberg, D. Williams-Young, F. Ding, F. Lipparini, F. Egidi, J. Goings, B. Peng, A. Petrone, T. Henderson, D. Ranasinghe, V. G. Zakrzewski, J. Gao, N. Rega, G. Zheng, W. Liang, M. Hada, M. Ehara, K. Toyota, R. Fukuda, J. Hasegawa, M. Ishida, T. Nakajima, Y. Honda, O. Kitao, H. Nakai, T. Vreven, K. Throssell, J. A. Montgomery, Jr., J. E. Peralta,

- F. Ogliaro, M. J. Bearpark, J. J. Heyd, E. N. Brothers, K. N. Kudin, V. N. Staroverov, T. A. Keith, R. Kobayashi, J. Normand, K. Raghavachari, A. P. Rendell, J. C. Burant, S. S. Iyengar, J. Tomasi, M. Cossi, J. M. Millam, M. Klene, C. Adamo, R. Cammi, J. W. Ochterski, R. L. Martin, K. Morokuma, O. Farkas, J. B. Foresman, D. J. Fox, Gaussian, Inc., Wallingford CT, 2016.
- [16] Wolfram Research, Inc., *Mathematica, Version 12.3*, Champaign, IL 2021.
- [17] M. J. Frisch, M. Head-Gordon, J. A. Pople, *Chem. Phys. Lett.* **1990**, *166*, 275–280.
- [18] M. Head-Gordon, J. A. Pople, M. J. Frisch, *Chem. Phys. Lett.* **1988**, *153*, 503–506.
- [19] M. J. Frisch, A. Pople, J. S. Binkley, *J. Chem. Phys.* **1984**, *80*, 3265–3269.
- [20] A. V. Marenich, C. J. Cramer, D. G. Truhlar, *J. Phys. Chem. B* **2009**, *113*, 6378–6396.
- [21] J. Pople, S. Binkley, R. Seeger, *Int. J. Quantum Chem.* **1976**, *10*, 1–19.
- [22] K. Raghavachari, J. A. Pople, *Int. J. Quantum Chem.* **1978**, *14*, 91–100.
- [23] K. Raghavachari, M. J. Frisch, J. A. Pople, *J. Chem. Phys.* **1980**, *72*, 4244–45.
- [24] K. Raghavachari, J. S. Binkley, R. Seeger, J. A. Pople, *J. Chem. Phys.* **1980**, *72*, 650–654.
- [25] J. R. Cheeseman, G. W. Trucks, T. A. Keith, M. J. Frisch, *J. Chem. Phys.* **1996**, *104*, 5497–509.
- [26] K. Wolinski, J. F. Hilton, P. Pulay, *J. Am. Chem. Soc.* **1990**, *112*, 8251–60.
- [27] W. Deng, J. R. Cheeseman, M. J. Frisch, *J. Chem. Theory Comput.* **2006**, *2*, 1028–1037.
- [28] A. D. Becke, *J. Chem. Phys.* **1993**, *98*, 5648–5652.
- [29] A. D. Becke, *J. Chem. Phys.* **1993**, *98*, 1372–1377.
- [30] C. Lee, W. Yang, R. G. Parr, *Phys. Rev. B* **1988**, *37*, 785–789.
- [31] B. Miehlich, A. Savin, H. Stoll, H. Preuss, *Chem. Phys. Lett.* **1989**, *157*, 200–206.
- [32] A. D. Becke, *Phys. Rev. A* **1988**, *38*, 3098–3100.
- [33] R. A. Kendall, T. H. Dunning Jr., R. J. Harrison, *J. Chem. Phys.* **1992**, *96*, 6796–806.
- [34] B. Jameson, R. Glaser, Experimental Determination of the Internal Rotation-Inversion Energy Barrier of tert-butyl (4-hydroxybutyl)(2,2,2-trifluoroethyl) tert-butyl carbamate. To Be Published.
- [35] J. Kincaid, H. Eyring, A. Stearn, *Chem. Rev.* **1941**, *28*, 301–365.
- [36] A. Allerhand, H. S. Gutowsky, J. Jonas, R. A. Meinzer, *J. Am. Chem. Soc.* **1966**, *88*, 3185–3194.
- [37] K. Wiberg, P. Rablen, D. Rush, T. Keith, *J. Am. Chem. Soc.* **1995**, *117*, 4261–4270.
- [38] T. Drakenberg, K. Dahlqvist, S. Forsén, *J. Phys. Chem.* **1972**, *76*, 2178–2183.
- [39] D. Kost, H. Egozy, *J. Org. Chem.* **1989**, *54*, 4909–4913.
- [40] R. Glaser, C. Horan, E. Nelson, M. Hall, *J. Org. Chem.* **1992**, *57*, 215–228.
- [41] K. B. Wiberg, W. F. Bailey, K. M. Lambert, *J. Org. Chem.* **2019**, *84*, 5783–5789.
- [42] R. Taylor, O. Kennard, *J. Am. Chem. Soc.* **1982**, *104*, 5063–5070.
- [43] A. G. Keller, P. A. Szczecinski, *RSC Adv.* **2014**, *4*, 27290–27296.

Manuscript received: June 24, 2022

Revised manuscript received: October 3, 2022

Version of record online: October 27, 2022